

Modulating internal electric field by oxygen vacancy engineering and consequent forming quantum wells for boosted selective CO₂ photoreduction

Xian Shi ^{a,1}, Weidong Dai ^{e,1}, Yang Bai ^{c,*}, Guilian Luo ^a, Xing'an Dong ^d, Qin Ren ^e, Liqun Ye ^{b,*}

^a School of Chemistry and Environmental Engineering, Sichuan University of Science & Engineering, Zigong 643000, China

^b College of Materials and Chemical Engineering, Key Laboratory of Inorganic Nonmetallic Crystalline and Energy Conversion Materials, China Three Gorges University, Yichang 443002, China

^c State Key Laboratory of Oil and Gas Reservoir Geology and Exploitation, School of Oil & Natural Gas Engineering, Southwest Petroleum University, Chengdu 610500, China

^d Chongqing Key Laboratory of Photo-Electric Functional Materials, College of Physics and Electronic Engineering, Chongqing Normal University, Chongqing 401331, China

^e Research Center for Environmental and Energy Catalysis, Institute of Fundamental and Frontier Sciences, University of Electronic Science and Technology of China, Chengdu 611731, China



ARTICLE INFO

Keywords:

Internal electric field
Oxygen vacancy engineering
Carrier separation
CO₂ photoreduction
Product selectivity

ABSTRACT

Although internal electric field of photocatalysts is considered as the potent driving force for efficient charge separation, modulating the internal electric field intensity remains a challenge. Herein, we considered that the internal electric field intensity of Sillén-structured bimetallic oxyhalide PbBiO₂Cl could be modulated by tuning surface oxygen vacancy concentration, thereby influencing the corresponding charge transfer. In comparison to bulk PbBiO₂Cl and PbBiO₂Cl with deficient oxygen vacancies, the PbBiO₂Cl with rich oxygen vacancies possessed enhanced internal electric field intensity due to its high oxygen vacancy concentrations, resulting in the primary charge separation spatially. Then the surface oxygen vacancies captured more dissociative electrons as quantum wells to promote the photocatalytic selective CO₂-CO conversion. The mechanism was researched and verified by in-situ FTIR and DFT calculations. Using defect engineering to simultaneously modulate internal electric field and form quantum wells for promoting charge separation is an efficient strategy to rationally improve photocatalytic performances.

1. Introduction

CO₂ photoreduction is one of the most promising technologies to control solve energy crisis in recent years [1,2]. Photogenerated charge transfer plays a vital role in photocatalytic redox reaction, which can efficiently improve CO₂ photoreduction activities and modulating product selectivity [3–5]. Therefore, it is important to find efficient strategies to improve the photoinduced charge separation efficiency of photocatalysts. A series of common strategies including heterostructure construction, element or ion group doping have been carried out to facilitate efficient carrier separation [6–8]. In addition to the external drive mentioned above, the intrinsic built-in internal electric fields of photocatalysts are deemed a native and potent driving force to improve

the charge transfer and separation, thereby enhancing the photocatalytic performances [9,10]. However, modulating internal electric field intensity in photocatalysts for CO₂ photoreduction has been rarely systematic studied.

Recently, the layered bismuth oxyhalides (BiOX, X = Cl, I, Br) with covalent metal oxygen layers ([Bi₂O₂]²⁺) separated by halide layers (X) have attracted much attention because of their widely application in the field of CO₂ photoreduction [11,12]. And the existence of intrinsic built-in internal electric field in BiOX due to the asymmetrical layered structures has been verified [13]. However, during the photocatalysis, it has been found that the structure of [Bi₂O₂]²⁺ layers and interleaved X double slabs enables the BiOX easy to be photocorrosion, which limits the further development of BiOX [14]. To address this situation, a part of

* Corresponding authors.

E-mail addresses: baiyang220523@126.com (Y. Bai), lqye@ctgu.edu.cn (L. Ye).

¹ These authors contributed equally to this work.

Bi atoms of the $[Bi_2O_2]^{2+}$ are replaced by other metal elements, forming the covalent bimetallic oxide ion layer ($[MBiO_2]^+$, M = Pb, Cd, Sr, Ba, etc). Among the above mentioned substitution atoms, the radius of Pb^{2+} is similar to that of Bi^{3+} , resulting in the crystal structure of $PbBiO_2X$ do not change greatly compared with $BiOX$. Moreover, the build of $PbBiO_2X$ can shorten the interlayer distance between $[PbBiO_2]^-$ and X layers, improving the interaction between $[PbBiO_2]^-$ and X' layers, thus enhancing the structural stability [15–17]. The shortened interlayer distance is also beneficial to the diffusion paths of photogenerated carriers, however, it may also lead to the recombination of photogenerated carriers, which hinders the further improvement of its photocatalytic performances [18–20]. Enhancing the internal electric field intensity may be a promising strategy to solve above issue. Therefore, finding efficient strategies to improve internal electric field of $PbBiO_2X$ for reducing the charge recombination is worthy of systematic studied.

Herein, Sillén-structured bimetallic oxyhalide $PbBiO_2Cl$ with different surface oxygen vacancy (OV) concentration have been successfully designed and synthesized, which were applied to CO_2 photoreduction. The fact that the internal electric fields of as prepared samples can be regulated by OV concentrations has been verified. Compared with the bulk $PbBiO_2Cl$ (PBOC) and $PbBiO_2Cl$ with deficient oxygen vacancies (PBOC-DOV), the strongest internal electric field of $PbBiO_2Cl$ with rich OV (PBOC-ROV) was confirmed by Kelvin probe force microscopy. The enhanced internal electric field as the driving force would firstly separate the photocharges, thus more dissociative electrons could migrate to the surface of PBOC-ROV. Then the electrons would be captured by surface OVs as quantum wells, further promoting the photogenerated carrier separation and supporting the favorable CO_2 photoreduction activity. Thus the CO_2 molecules would be adsorbed on OVs, activated and then selective reduced by accumulated electrons in OVs as active sites. Generally, researches on surface vacancies of photocatalysts is mostly focused on their use as quantum wells, this work will provide an in-depth understanding of defect engineering. Meanwhile, modulating internal drive of photocatalysts and forming stable active sites via defect engineering should be an efficient strategy for sustainable and stable photocatalytic energy conversion.

2. Experimental methods

2.1. Sample preparation

PBOC-ROV: 0.17 g of $Pb(NO_3)_2$ and 0.16 g of N-Hexadecyltrimethylammonium Chloride ($C_{19}H_{42}ClN$) were primarily dissolved in 20 mL of ethanol, and 0.24 g of $Bi(NO_3)_3 \cdot 5 H_2O$ was dissolved into above solution under 30 min continuous stirring. Then 0.2 g of polyvinyl pyrrolidone (PVP-K30) was added. After stirring for 1 h, pouring above solution into a 50 mL Teflon-lined autoclave and heated it at 160 °C for 24 h. After reaction, the precipitate was cleaned by ethanol and deionized water for 5 times and then vacuum dried at 80 °C for 24 h.

PBOC-DOV: 20 mL of deionized water was poured into a 50 mL Teflon-lined autoclave. 0.5 g of PBOC-ROV sample was fully dispersed. After heating it at 160 °C for 4 h, the obtained sample was cleaned by ethanol and deionized water for 5 times and then vacuum dried at 80 °C for 24 h.

Bulk PBOC: The synthesis steps and chemical reagents used for bulk PBOC preparation were the same as those of PBOC-ROV preparation, except for adding 10 mL of $NH_3 \cdot H_2O$ before high-temperature heating, the $NH_3 \cdot H_2O$ was used to enable the sample to form bulk structure according to the previous report [18].

2.2. CO_2 photoreduction

10 mg of photocatalyst, 1 mL of deionized water and 1 atm pure CO_2 gas were used to evaluate CO_2 photoreduction activity in a reactor of the Labsolar 6 A system equipped with a 300 W xenon lamp with an AM 1.5 G filter as the light source. The reaction temperature was controlled by

circulation cooling system at 298 K. The CO_2 photoreduction gas was detected and analyzed by a gas chromatograph. The yield rate of the gaseous product [$\phi(gas)$] and the product selectivity were calculated by the empirical formulas. The detailed experimental operations, analysis of experimental results and instrument types were described in the Supporting Information.

2.3. In-situ FTIR spectroscopy

The photocatalytic mechanism was analyzed by the intermediates produced during CO_2 photoreduction process using the in-situ FTIR spectroscopy under light irradiation by a 300 W xenon lamp with an AM 1.5 G filter. The dynamic adsorption and reduction processes were recorded by FTIR spectra. The detailed experimental operations and instrument types were described in the Supporting Information.

3. Results and discussion

3.1. Structural characterizations, CO_2 photoreduction ability and product selectivity of PBOCs with different OV concentrations

The PBOC-ROV was prepared via a self-assembly method using $C_{19}H_{42}ClN$ and PVP-K30 complex acted as the reactant, solvent, and capping agent. The complex system formed of a passivation layer around sample, which hindered the further growth of the sample. Under hydrothermal conditions, the OVs on the surface of the PBOC-ROV could be repaired by oxygen in the water to prepare PBOC-DOV. The HRTEM images of PBOC-ROV exhibited good crystallinity (Fig. 1a), some lattice disorder of PBOC-ROV was shown in Fig. 1b due to more surface OVs generation, and the interplanar distance of the continuous lattice fringes was 0.28 nm, which matched well with the (020) atomic planes of tetragonal $PbBiO_2Cl$ (Figs. 1a and 1c) [21,22]. The relevant morphology and interplanar lattice spacing of PBOC and PBOC-DOV were shown in Figs. S1 to S4. The XRD patterns of Sillén-structured PBOC photocatalysts with tunable surface vacancy concentrations were shown in Fig. 1d. A series of diffraction peaks were ascribed to the tetragonal $PbBiO_2Cl$ (JCPDS No. 13-0352). The (002) peak shift of PBOCs with different surface vacancy concentrations toward smaller angles was due to the residual stress induced by the surface vacancies on PBOCs [22]. In order to confirm the surface vacancies type, the low-temperature EPR analysis was used to detect the signals of the surface vacancies. It could be observed from Fig. 1e that the EPR signal at $g = 2.001$ was ascribed to the free electrons trapped by surface OVs [23–25]. The PBOC-ROV exhibited the strongest EPR signal intensity, while the bulk PBOC showed the negligible EPR signal intensity, suggesting PBOC-ROV contained the highest OV concentration, followed by PBOC-DOV and then bulk PBOC. The high resolution O 1 s XPS spectra was presented in Fig. 1f. The peaks located at 528.9 and 530.9 eV belonged to the lattice oxygen (Bi-O or Pb-O) and surface hydroxyl groups, respectively. As for PBOC-DOV and PBOC-ROV, the peaks at 530.0 eV were ascribed to O atoms in the vicinity of OVs, and the OVs proportion in PBOC-ROV was larger than those of PBOC-DOV and bulk PBOC, which matched well with EPR results [21]. The high resolution Pb 4 f, Bi 4 f and Cl 2p XPS spectra of PBOCs were shown in Figs. S5–S7, it could be observed and confirmed from the results that the related peaks of Pb 4 f and Bi 4 f of the PBOC-ROV all possessed an obvious red-shift, which was due to the fracture of Pb-O or Bi-O bonds induced by increasing OV concentration compared with PBOC-DOV and bulk PBOC [22]. Above results demonstrated the evidence that more OVs were introduced to PBOC-ROV.

The optical absorption and bandgaps of the as prepared PBOCs were determined by UV-vis DRS spectra. As shown in Fig. S8, the absorption bands of the PBOC-ROV, PBOC-DOV and bulk PBOC were at 572.3, 499.1 and 483.5 nm, respectively. An extend absorption band edge due to the increase in the OV concentrations was observed [26]. The Tauc plot of the PBOCs was shown in Fig. S9. The bandgaps of PBOC-ROV, PBOC-DOV and bulk PBOC were 1.74, 2.15 and 2.28 eV, respectively,

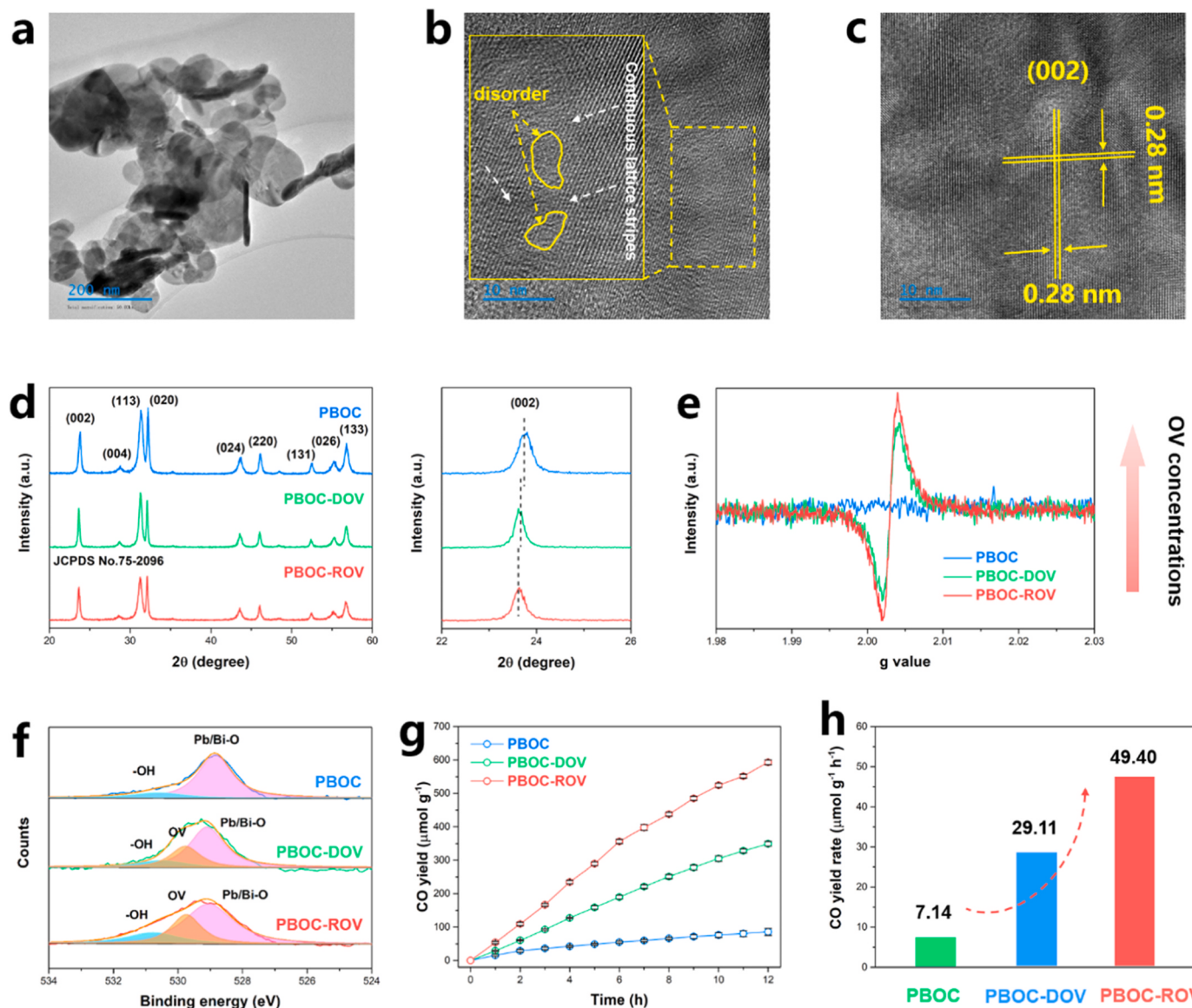


Fig. 1. Structural characterization, CO_2 photoreduction ability and product selectivity of PBOCs. (a-c) High-resolution transmission electron microscope (HRTEM) images of PBOC-ROV, (d) X-ray diffraction (XRD) patterns of PBOC, PBOC-DOV and PBOC-ROV, (e) electron paramagnetic resonance (EPR) of PBOC, PBOC-DOV and PBOC-ROV, (f) O 1 s X-ray photoelectron spectroscopy (XPS) of PBOC, PBOC-DOV and PBOC-ROV, (g, h) CO_2 photoreduction performances of PBOC, PBOC-DOV and PBOC-ROV.

indicating that more surface OVs could narrow the bandgap of the PBOC. The valence band positions of PBOC-ROV, PBOC-DOV and bulk PBOC were determined by valence-band XPS spectra in Fig. S8, which were at 1.14, 0.85 and 0.63 eV, respectively (Fig. S10).

The CO_2 photoreduction activity of photocatalysts were evaluated in pure water and no sacrificial agent or photosensitizer was used during the reaction. As shown in Figs. 1g and 1h, in the 12-h photoreaction, only gaseous CO as the product was detected by gas chromatography, indicating that the product selectivity of CO_2 photoreduction achieved 100 %. The bulk PBOC was almost inactive to CO_2 photoreduction process. The PBOC-ROV exhibited an enhanced CO_2 photoreduction activity with a CO yield rate of $49.40 \mu\text{mol g}^{-1} \text{h}^{-1}$, which was 1.7 and 6.9 times higher than those of the PBOC-DOV ($29.11 \mu\text{mol g}^{-1} \text{h}^{-1}$) and bulk PBOC ($7.14 \mu\text{mol g}^{-1} \text{h}^{-1}$), respectively. Meanwhile, CH_4 and H_2 were not detected during photoreduction process (Figs. S11 and S12). Meanwhile, no product was detected in the control experiments in dark, in Ar atmosphere, or without photocatalysts, suggesting the formation of CO was from CO_2 photoreduction (Figs. S13 to S14) [27]. Furthermore,

the ^{13}C isotope labeling experiment proved the generated CO was originated from CO_2 reduction (Fig. S15). After the CO_2 photoreduction reaction, the crystal structure and surface OVs of the PBOC-ROV were tested by XRD and EPR, respectively (Figs. S16 and S17), no obvious changes were found compared with the pristine sample, indicating the stable crystal structure and surface OVs. Owing to more OVs formed on the surface, PBOC-ROV showed enhanced CO_2 photoreduction performance. The effect of OVs on photocatalysis promotion was further explored next step.

3.2. The relationship between internal electric field intensity and surface OV concentrations over PBOC catalysts

The internal electric field intensity of PBOCs were investigated in light of the surface OV concentrations, and the examination revealed that the surface OV-rich structure regulated the internal electric field intensity [13]. The internal electric field intensity of PBOCs could be calculated based on the surface potential. The surface potentials were

measured through the KPFM, and the average surface potential of PBOC-ROV, PBOC-DOV and PBOC were measured as 751.3, 665.9, and 346.1 mV, respectively (Figs. 2a to 2f, S18). This indicated that the internal electric field intensity of PBOCs was raised with increasing concentration of surface OVs. Moreover, the measured transient photocurrent density was integrated by subtracting the steady-state value of the photocurrent with respect to time, which was proportional to the amount of positive charges accumulated on the surface of the photocatalyst. We measured the transient photocurrent and integrated the peaks of the transient anode photocurrent (Fig. 2g). The surface charge density of bulk PBOC, PBOC-DOV and PBOC-ROV was 1.94, 2.13 and $33.39 \mu\text{C cm}^{-2}$, respectively, which matched well with the KPFM results. An enhanced internal electric field intensity of PBOC-ROV could be reflected by its highest surface charge density.

The internal electric field magnitude of PBOCs could be calculated using the following empirical equation [28]:

$$F_s = (-2 V_s \rho / \epsilon \epsilon_0)^{1/2}$$

Where F_s was the internal electric field magnitude, V_s was the surface voltage, ρ was the surface charge density, ϵ was the low-frequency dielectric constant, and ϵ_0 was the permittivity of free space. It was known that internal electric field intensity was mainly confirmed by the charge density and surface voltage. In order to evaluate the internal

electric field intensity of PBOCs, the surface voltages measured by open-circuit potentials tests were finished (Fig. 2h). As shown in Fig. 2i, it could be calculated that the internal electric field intensity of PBOC-ROV was 7.38 and 5.47 times as high as those of PBOC-DOV and bulk PBOC, respectively (assuming internal electric field intensity of bulk PBOC to be '1'). Above results confirmed the enhanced internal electric field intensity of PBOC-ROV due to its highest surface OV concentrations. And the enhanced internal electric field intensity of PBOC-ROV was the potent driving force for spatial transfer and separation of photoinduced charge carriers, which was the primary feature supporting its improved CO_2 photoreduction performance.

3.3. Effects of surface OVs as quantum wells on CO_2 photoreduction

In addition to modulating the internal electric field intensity, the role of surface OVs as quantum wells to further accelerate carrier separation via capturing electrons was confirmed in this part. Benefit from the enhanced internal electric field intensity, more photoexcited electrons would be pumped to the conduction band firstly. Moreover, the photo-induced electrons on conduction band captured by surface OVs was profit for charge separation, which could be proved by optoelectronic properties of PBOCs. The EIS confirmed that PBOC-ROV exhibited the smallest radius in Fig. 3a [29]. Meanwhile, the PBOC-ROV possessed the

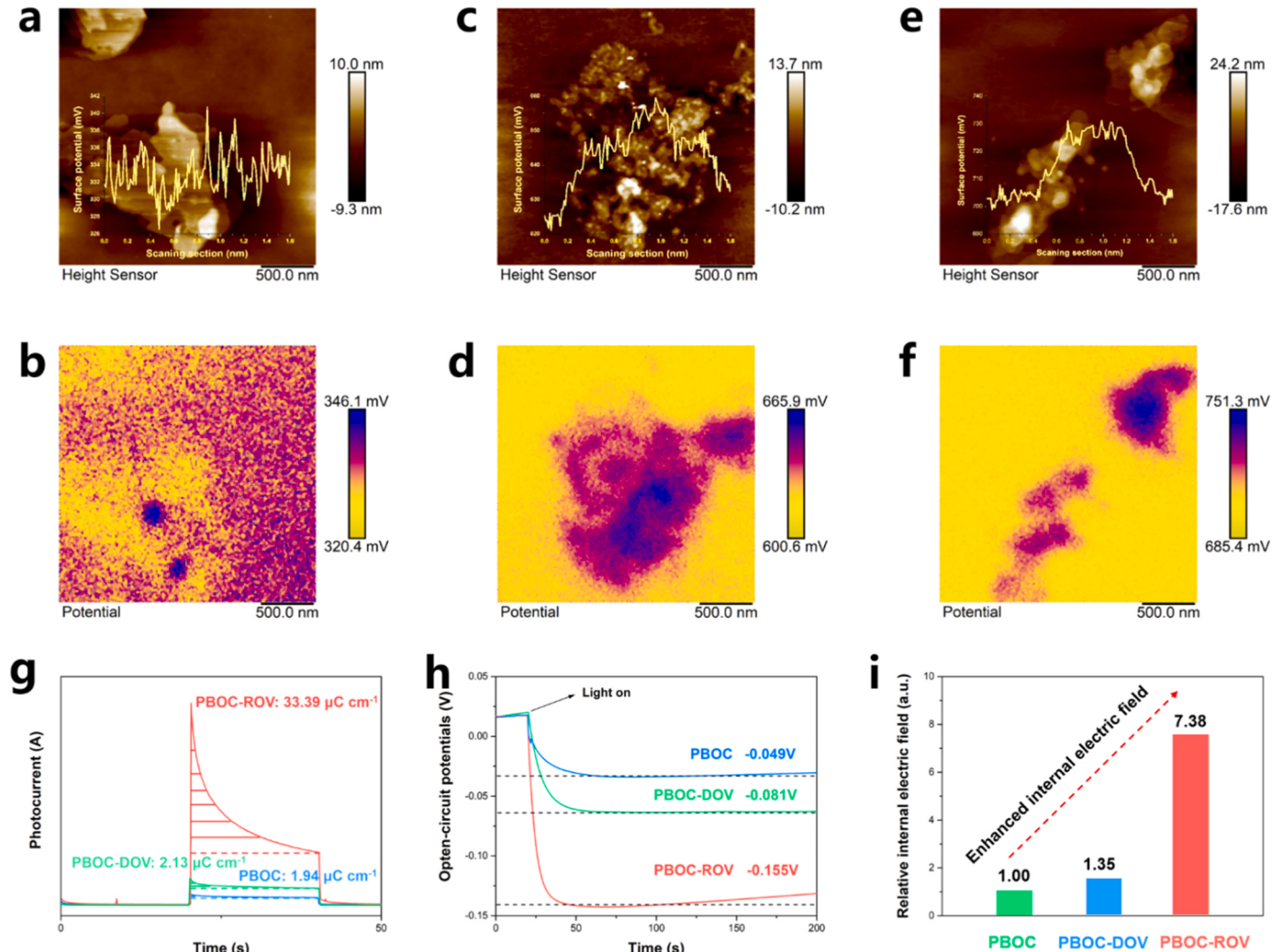


Fig. 2. Internal electric field intensity influenced by surface OV concentrations. (a, c, e) Atomic force microscopy (AFM) images and (b, d, f) the corresponding surface potential measured by Kelvin probe force microscopy (KPFM) of PBOCs, (g) the transient photocurrent density of PBOCs for surface charge density calculation, (h) the open-circuit potentials of PBOCs and (i) corresponding calculated internal electric field intensity.

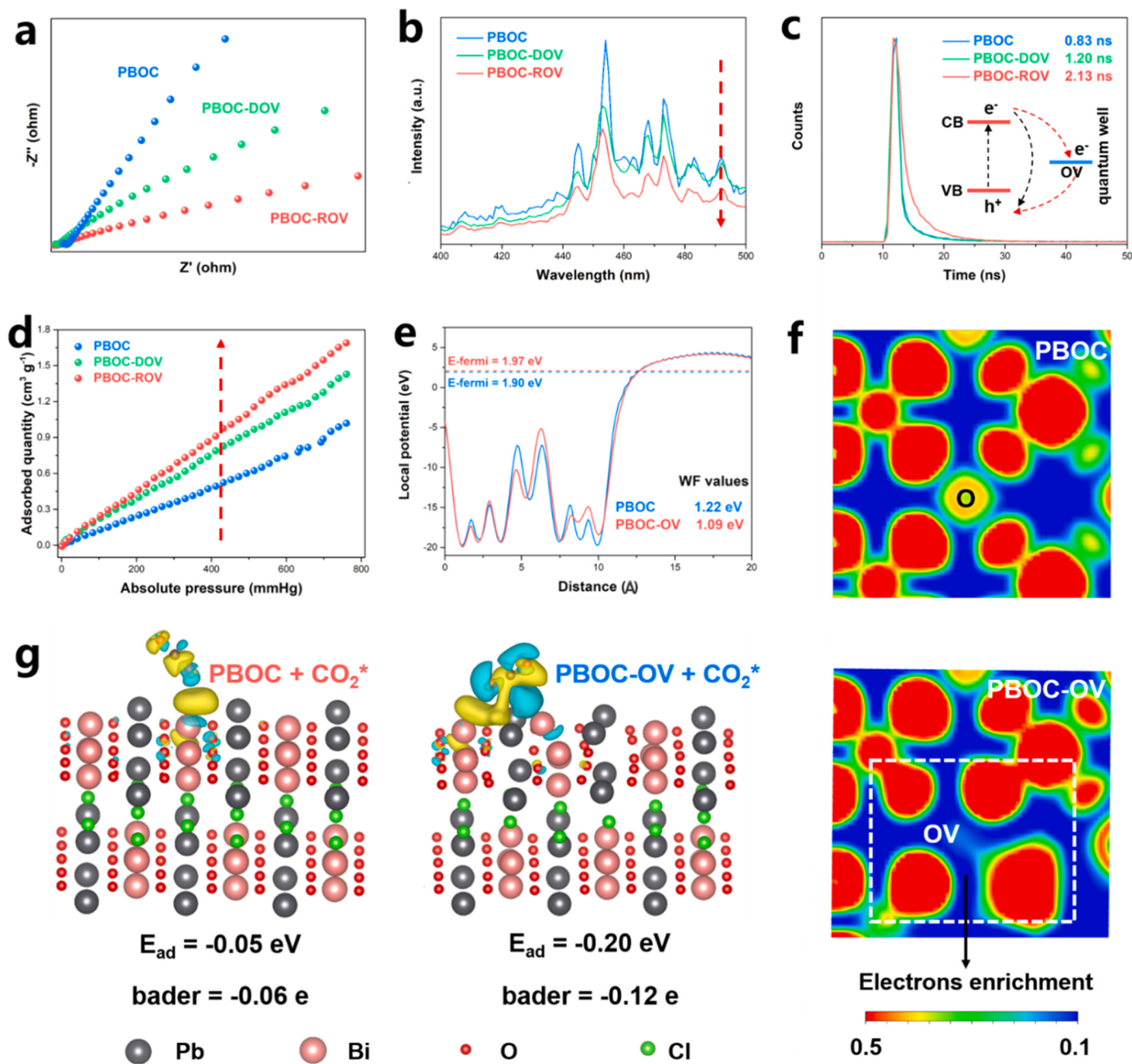


Fig. 3. Effects of surface OVs as quantum wells on CO_2 photoreduction. (a) Electrochemical impedance spectra (EIS) images of PBOCs, (b) photoluminescence (PL) spectra and (c) time-resolved transient PL decay, (d) CO_2 adsorption isotherms at 25 °C of PBOCs, (e) the electronic work functions (WFs) of PBOCs, (f) electron Localization Function (ELF) of PBOC and PBOC-OV surface, (g) CO_2 adsorption, charge density and bader values simulated by DFT of PBOCs, E_{ad} represented the adsorption energy, the isosurfaces were set to 0.00025 e \AA^{-1} , the negative values of bader analysis indicated the CO_2 gained electrons.

highest photocurrent intensity among the samples followed by PBOC-DOV and bulk PBOC (Fig. S19) [30]. Above results indicated the lowest charge-transfer resistance of PBOC-ROV, resulting in the enhanced photogenerated carriers separation and transfer [31,32]. The steady-state PL spectra in Fig. 3b showed that the PBOC-ROV expressed the lowest intensity among the samples, which also suggested more OVs on PBOC-ROV could efficiently hinder the recombination of photogenerated charges [33]. As shown in Fig. 3c, time-resolved PL spectroscopy revealed that bulk PBOC possessed a single lifetime component, which was assigned to a direct recombination of photogenerated electron and hole pairs, displaying a lifetime of 0.83 ns (τ (PBOC)). As the OV concentrations increased, the lifetime of charge carriers of PBOC-DOV was 1.20 ns. While for PBOC-ROV, the lifetime of

charge carriers was further extend to 2.13 ns because more surface OVs transiently trapped photoelectrons as quantum wells. Impressively, PBOC-ROV displayed the longest lifetime among the samples, indicating that higher concentration of OVs firstly enhanced internal electric field intensity for improving photoinduced carrier separation, and then provided more competent quantum wells to further inhibit the recombination of charges.

The abilities of PBOCs to adsorb and capture CO_2 was regarded as an important factor for photocatalysis. The improved CO_2 adsorption ability of PBOCs was confirmed by CO_2 adsorption isotherms. As shown in Fig. 3d, PBOC-ROV exhibited strongest CO_2 adsorption ability among the samples. However, the Brunauer-Emmett-Teller results (Fig. S20) demonstrated that PBOCs possessed similar specific surface area. Above

results suggested that the CO_2 capture capability was affected by the surface OV concentrations on photocatalysts. The effects of OVs on CO_2 photoreduction were further explored by DFT calculations. The WFs of PBOC surface without OV (PBOC) and with one OV (PBOC-OV) were calculated as 1.22 eV and 1.09 eV (Fig. 3e), respectively. A lower barrier for photoexcited electron transfer could be confirmed by the smaller calculated WF value of PBOC-OV, this was consistent with the experimental results that internal electric field intensity was enhanced by increasing surface OV concentrations. It was noted from the ELF in Fig. 3f that a certain amount of electrons was enriched near the OV of PBOC-OV structure compared with PBOC structure, indicating that the OVs on PBOC were quantum wells for trapping electrons and enhancing the carrier separation, which was in agreement with above results. As shown in Fig. 3g, the CO_2 adsorption energy of PBOC and PBOC-OV was -0.05 eV and -0.20 eV, respectively, which was in agreement with CO_2 adsorption experimental results. The charge density difference indicated a stronger interaction between the CO_2 molecule and vacancy in PBOC-OV than PBOC at the same plotting scale. The bader analysis further demonstrated that the adsorbed CO_2 gained more electrons (0.12 e) from PBOC-OV than that adsorbed on PBOC (0.06 e), which was favorable for CO_2 activation and reduction.

3.4. Reaction mechanism and kinetics for CO_2 photoreduction induced by OVs

In-situ FTIR measurement was used to explore and confirm the selective photoreduction pathway. As shown in Figs. 4a to 4c, the IR peak intensity of PBOC-ROV at 1327.3 and 1524.3 cm^{-1} expressed a more obvious increase with the prolonged light irradiation time than those of bulk PBOC and PBOC-DOV, indicating the generation of the COOH^* , which was considered as a crucial intermediate of the photoreduction from CO_2 to CO [34–39]. The generation of COOH^* was also the rate-limiting step of the selective CO_2 photoreduction. This step that proceeded on PBOC was endothermic, the energy barrier was calculated as $+0.10$ eV. After introducing one OV, the energy barrier of this step for PBOC-OV was decreased to -0.07 eV, indicating that the OV transformed the reaction from endothermic to exothermic, suggesting that OV was more conducive to COOH^* generation. This was because the adsorbed CO_2 was continuously reduced by more incoming electron-transfer promoted by OVs, and the successive protonation process was promoted (Figs. 4d, S21 and S22, Tables S1 and S2) [40]. The effect of surface OVs on PBOC for boosted CO_2 photoreduction was revealed on basis of experimental results as follows (Fig. 4e): the internal electric field intensity of PBOC was efficiently enhanced by increasing surface OV concentrations, which firstly promoted the carrier separation. More photoinduced electrons were captured by surface OVs as quantum wells, leading to a further separation of photocharges. The CO_2

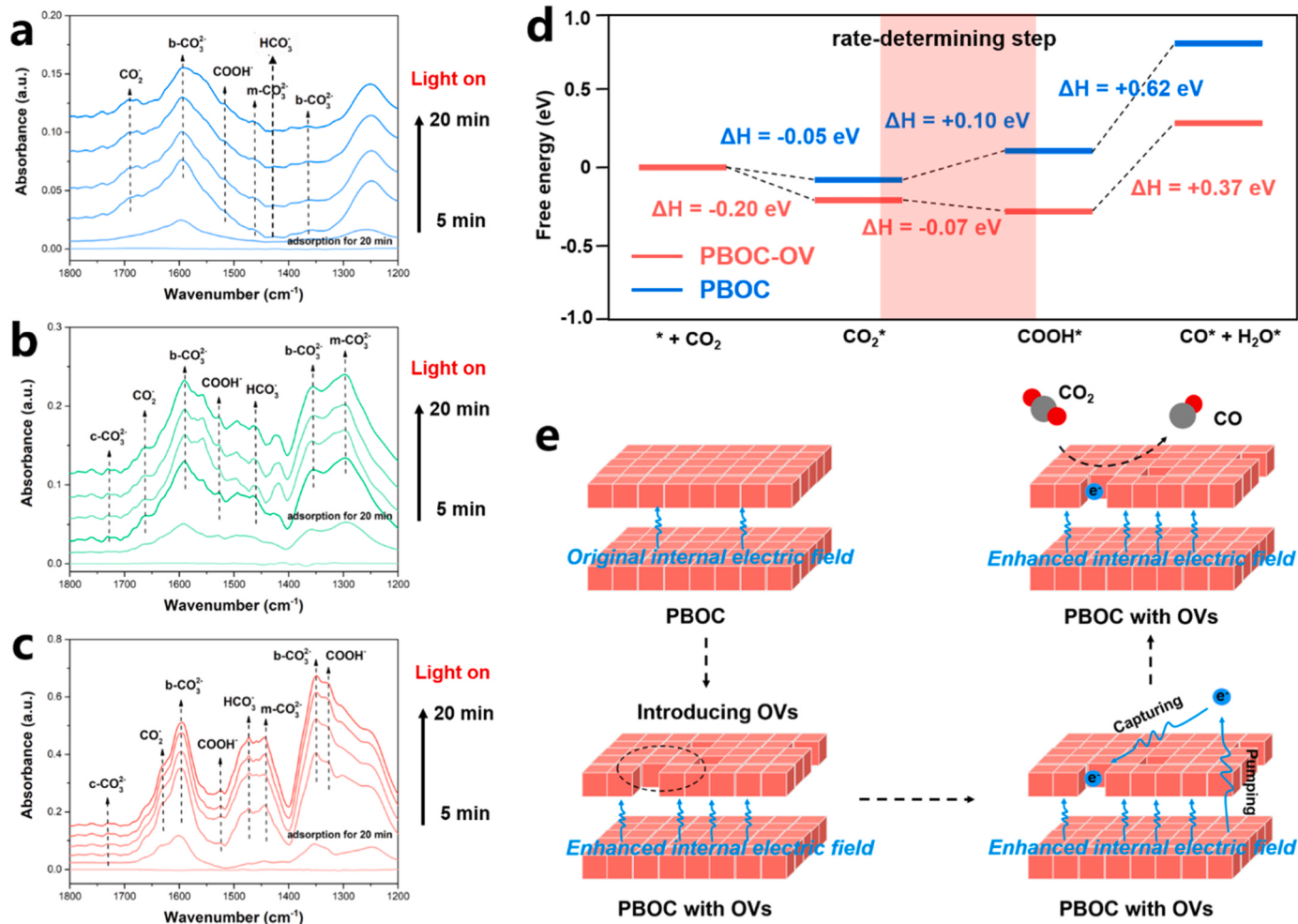


Fig. 4. Reaction mechanism and kinetics for CO_2 photoreduction induced by OVs. (a-c) In-situ Fourier-transform infrared spectroscopy (FTIR) of CO_2 photoreduction process of PBOCs, (d) reaction energy diagram of CO_2 reduction catalyzed by PBOC and PBOC-OV, the asterisk (*) demonstrated the adsorption sites on the substrates, (e) photocatalytic mechanism induced by enhanced internal electric field intensity via OVs introduction.

molecules adsorbed on surface OVs would directly interact with the protons from H_2O , and more COOH^* was generated in this step with a lower energy barrier, finally leading to the CO generation as the product with a 100% selectivity.

4. Conclusions

In summary, through the experimental and DFT calculation results obtained in this work, we confirmed that the surface OV concentrations of PbBiO_2Cl could effectively modulate the internal electric field intensity, promoting the primary photocharge transfer and separation. The rich OVs not only improved the internal electric field intensity, but also serve as the quantum wells to capture photoinduced electrons, leading to a further enhanced carrier separation. More dissociative electrons captured by OVs were injected to adsorbed CO_2 molecules, thus promoting an enhanced CO_2 activation and selective photocatalytic conversion of CO_2 into CO with a lower energy barrier of COOH^* generation as the rate-limiting step. This work revealed the oxygen vacancy engineering to promote CO_2 photoreduction via internal electric field intensity modulation and active site generation provided an efficient strategy for designing high-efficient photocatalytic materials for solar energy conversion.

CRediT authorship contribution statement

Xian Shi, Weidong Dai, Yang Bai, and Liqun Ye: Formal analysis, Methodology, Investigation, Writing – original draft. **Xing'an Dong and Guilian Luo:** Methodology, Validation, Investigation. **Qin Ren:** Investigation, Methodology. **Xian Shi and Liqun Ye:** Conceptualization, Supervision, Project administration, Funding acquisition.

Declaration of Competing Interest

The authors declare that they have no competing interests.

Data availability

Data will be made available on request.

Acknowledgements

This work was supported by National Natural Science Foundation of China (No. 52200123, No. 51872147), Hubei Provincial Natural Science Foundation of China (No. 2022CFA065), the 111 Project (D20015).

Appendix A. Supporting information

Supplementary data associated with this article can be found in the online version at [doi:10.1016/j.apcatb.2023.123523](https://doi.org/10.1016/j.apcatb.2023.123523).

References

- [1] A. Wagner, C. Sahm, E. Reisner, Towards molecular understanding of local chemical environment effects in electro- and photocatalytic CO_2 reduction, *Nat. Catal.* 3 (2020) 775–786.
- [2] Y. Zhang, L. Tao, C. Xie, D. Wang, Y. Zou, R. Chen, Y. Wang, C. Jia, S. Wang, Defect engineering on electrode materials for rechargeable batteries, *Adv. Mater.* 32 (2020), 1905923.
- [3] J. Di, C. Chen, S. Yang, S. Chen, Z. Liu, Isolated single atom cobalt in $\text{Bi}_3\text{O}_4\text{Br}$ atomic layers to trigger efficient CO_2 photoreduction, *Nat. Commun.* 10 (2019) 2840–2846.
- [4] X. Li, J. Yu, M. Jaroniec, X. Chen, Cocatalysts for selective photoreduction of CO_2 into solar fuels, *Chem. Rev.* 119 (2019) 3962–4179.
- [5] C. Gao, Q. Meng, K. Zhao, H. Yin, D. Wang, J. Guo, S. Zhao, L. Chang, M. He, Q. Li, H. Zhao, X. Huang, Y. Gao, Z. Tang, Co_3O_4 hexagonal platelets with controllable facets enabling highly efficient visible-light photocatalytic reduction of CO_2 , *Adv. Mater.* 28 (2016) 6485–6490.
- [6] Q. Han, X. Bai, Z. Man, H. He, L. Li, J. Hu, A. Alsaedi, T. Hayat, Z. Yu, W. Zhang, J. Wang, Y. Zhou, Z. Zou, Convincing synthesis of atomically-thin, single-crystalline InVO_4 sheets toward promoting highly selective and efficient solar conversion of CO_2 into CO, *J. Am. Chem. Soc.* 141 (2019) 4209–4213.
- [7] Y. Zhao, G. Waterhouse, G. Chen, X. Xiong, L. Wu, C. Tung, T. Zhang, Two-dimensional-related catalytic materials for solar-driven conversion of CO_x into valuable chemical feedstocks, *Chem. Soc. Rev.* 48 (2019) 1972–2010.
- [8] H. Yu, J. Li, Y. Zhang, S. Yang, K. Han, F. Dong, T. Ma, H. Huang, Three-in-one oxygen vacancies: whole visible-spectrum absorption, efficient charge separation, and surface site activation for robust CO_2 photoreduction, *Angew. Chem. Int. Ed.* 58 (2019) 3880–3884.
- [9] H. Nguyen, A. Alzamly, Covalent organic frameworks as emerging platforms for CO_2 photoreduction, *ACS Catal.* 11 (2021) 9809–9824.
- [10] C. Qian, S. Wei, D. Hung, C. Qiu, G. Ozin, Catalytic CO_2 reduction by palladium-decorated silicon-hydride nanosheets, *Nat. Catal.* 2 (2018) 46–54.
- [11] H. Suzuki, H. Kunioku, M. Higashi, O. Tomita, D. Kato, H. Kageyama, R. Abe, Lead bismuth oxyhalides PbBiO_2X ($\text{X} = \text{Cl}, \text{Br}$) as visible-light-responsive photocatalysts for water oxidation: role of lone-pair electrons in valence band engineering, *Chem. Mater.* 30 (2018) 5862–5869.
- [12] J. Wu, X. Li, W. Shi, P. Ling, Y. Sun, X. Jiao, S. Gao, L. Liang, J. Xu, W. Yan, C. Wang, Y. Xie, Efficient visible-light-driven CO_2 reduction mediated by defect-engineered BiOB atomic layers, *Angew. Chem. Int. Ed.* 57 (2018) 1–7.
- [13] Z. Wu, W. Li, J. Xu, J. Jing, J. Li, J. Shen, L. Yang, W. Feng, S. Zhang, Y. Zhu, Internal electric field enhancement by the I-rich surface of highly crystallized BiOI nanosheets for boosted photocatalytic degradation of phenol, *Small Struct.* (2023), 2200380.
- [14] H. Lin, W. Lee, S. Huang, L. Chen, T. Yeh, J. Fu, C. Chen, Controlled hydrothermal synthesis of $\text{PbBiO}_2\text{Br}/\text{BiOI}$ heterojunction with enhanced visible-driven light photocatalytic activities, *J. Mol. Catal. A* 417 (2016) 168–183.
- [15] X. Li, J. Wang, D. Xu, Z. Sun, Q. Zhao, W. Peng, Y. Li, G. Zhang, F. Zhang, X. Fan, NbSe_2 Nanosheet supported PbBiO_2Br as a high performance photocatalyst for the visible light-driven asymmetric alkylation of aldehyde, *ACS Sustain. Chem. Eng.* 3 (2015) 1017–1022.
- [16] F. Liu, Y. Jiang, C. Chen, W. Lee, Novel synthesis of $\text{PbBiO}_2\text{Cl}/\text{BiOCl}$ nanocomposite with enhanced visible-driven-light photocatalytic activity, *Catal. Today* 300 (2018) 112–123.
- [17] J. Olchowka, H. Kabour, M. Colmont, M. Adlung, C. Wickleder, O. Mentré, ABiO_2X ($\text{A} = \text{Cd}, \text{Ca}, \text{Sr}, \text{Ba}, \text{Pb}; \text{X} = \text{halogen}$) selenite X1 series: polymorphism versus optical properties, *Inorg. Chem.* 55 (2016) 7582–7592.
- [18] Y. Xia, Z. He, J. Su, K. Hu, Polyacrylamide gel synthesis and photocatalytic performance of PbBiO_2Br nanosheets, *Mater. Lett.* 241 (2019) 64–67.
- [19] L. Wang, X. Zhao, D. Lv, C. Liu, W. Lai, C. Sun, Z. Su, X. Xu, W. Hao, S. Dou, Promoted photocharge separation in 2D lateral epitaxial heterostructure for visible-light-driven CO_2 photoreduction, *Adv. Mater.* (2020), 2004311.
- [20] Y. Zhang, B. Xia, J. Ran, K. Davey, S. Qiao, Atomic-level reactive sites for semiconductor-based photocatalytic CO_2 reduction, *Adv. Energy Mater.* 10 (2020), 1903879.
- [21] B. Wang, J. Di, P. Zhang, J. Xia, S. Dai, H. Li, Ionic liquid-induced strategy for porous perovskite-like PbBiO_2Br photocatalysts with enhanced photocatalytic activity and mechanism insight, *Appl. Catal. B Environ.* 206 (2017) 127–135.
- [22] B. Wang, W. Zhang, G. Liu, H. Chen, Y. Weng, H. Li, P. Chu, J. Xia, Excited electron-rich $\text{Bi}^{(3-x)+}$ sites: a quantum well-like structure for highly promoted selective photocatalytic CO_2 reduction performance, *Adv. Funct. Mater.* 32 (2022), 2202885.
- [23] Y. Li, M. Wen, Y. Wang, G. Tian, C. Wang, J. Zhao, Plasmonic hot electrons from oxygen vacancies for infrared light-driven catalytic CO_2 reduction on $\text{Bi}_2\text{O}_{3-x}$, *Angew. Chem. Int. Ed.* 133 (2021) 923–929.
- [24] F. Calaza, Y. Xu, D. Mullins, S. Overbury, Oxygen vacancy-assisted coupling and enolization of acetaldehyde on CeO_2 (111), *J. Am. Chem. Soc.* 134 (2012) 18034–18045.
- [25] J. Di, C. Chen, C. Zhu, R. Long, H. Chen, X. Cao, J. Xiong, Y. Weng, L. Song, S. Li, H. Li, Y. Xiong, Z. Liu, Surface local polarization induced by bismuth-oxygen vacancy pairs tuning non-covalent interaction for CO_2 photoreduction, *Adv. Energy Mater.* 11 (2021), 2102389.
- [26] S. Wang, X. Ding, X. Chang, Y. Meng, X. Yang, Z. Chen, J. Ye, Light-switchable oxygen vacancies in ultrafine $\text{Bi}_5\text{O}_7\text{Br}$ nanotubes for boosting solar-driven nitrogen fixation in pure water, *Adv. Mater.* 29 (2017), 28614603.
- [27] X. Shi, X. Dong, Y. He, P. Yan, S. Zhang, F. Dong, Photoswitchable chlorine vacancies in ultrathin $\text{Bi}_4\text{O}_5\text{Cl}_2$ for selective CO_2 photoreduction, *ACS Catal.* 12 (2022) 3965–3973.
- [28] X. Chen, Y. Xu, X. Ma, Y. Zhu, Large dipole moment induced efficient bismuth chromate photocatalysts for wide-spectrum driven water oxidation and complete mineralization of pollutants, *Natl. Sci. Rev.* 7 (2020) 652–659.
- [29] P. Li, Z. Zhou, Q. Wang, M. Guo, Y. Xiong, Visible-light-driven nitrogen fixation catalyzed by $\text{Bi}_5\text{O}_7\text{Br}$ nanostructures: enhanced performance by oxygen vacancies, *J. Am. Chem. Soc.* 142 (2020) 12430–12439.
- [30] F. Chen, H. Huang, L. Ye, T. Zhang, Y. Zhang, Thickness-dependent facet junction control of layered BiIO_3 single crystals for highly efficient CO_2 photoreduction, *Adv. Funct. Mater.* 28 (2018), 1804284.
- [31] S. Cao, B. Shen, T. Tong, J. Fu, J. Yu, 2D/2D heterojunction of ultrathin MXene/ Bi_2WO_6 nanosheets for improved photocatalytic CO_2 reduction, *Adv. Funct. Mater.* 28 (2018), 1800136.
- [32] Z. Xiong, X. Zhao, Nitrogen-doped titanate-anatase core-shell nanobelts with exposed {101} anatase facets and enhanced visible light photocatalytic activity, *J. Am. Chem. Soc.* 134 (2012) 5754–5757.
- [33] X. Dong, Z. Cui, Y. Sun, F. Dong, Humidity-independent photocatalytic toluene mineralization benefits from the utilization of edge hydroxyls in layered double

hydroxides (LDHs): a combined operando and theoretical investigation, *ACS Catal.* 11 (2021) 8132–8139.

[34] K. Niu, X. You, Y. Rong, H. Xin, L. Feng, C. Tuan, Y. Lum, K. Bustillo, M. Doeff, A spongy nickel-organic CO₂ reduction photocatalyst for nearly 100% selective CO production, *Sci. Adv.* 3 (2017) 786–787.

[35] Z. Guo, G. Chen, C. Cometto, B. Ma, M. Robert, Selectivity control of CO versus HCOO⁻ production in the visible-light-driven catalytic reduction of CO₂ with two cooperative metal sites, *Nat. Catal.* 2 (2019) 801–808.

[36] J. Sheng, Y. He, J. Li, C. Yuan, F. Dong, Identification of halogen-associated active sites on bismuth-based perovskite quantum dots for efficient and selective CO₂-to-CO photoreduction, *ACS Nano* 14 (2020) 13103–13114.

[37] X. Jiao, X. Li, X. Jin, Y. Sun, J. Xu, L. Liang, H. Ju, J. Zhu, Y. Pan, W. Yan, Y. Lin, Y. Xie, Partially oxidized SnS₂ atomic layers achieving efficient visible-light-driven CO₂ reduction, *J. Am. Chem. Soc.* 139 (2017) 18044–18051.

[38] L. Mino, G. Spoto, A. Ferrari, CO₂ capture by TiO₂ anatase surfaces: a combined DFT and FTIR study, *J. Phys. Chem. C* 118 (2014) 25016–25026.

[39] L. Cheng, D. Zhang, Y. Liao, J. Fan, Q. Xiang, Structural engineering of 3D hierarchical Cd_{0.8}Zn_{0.2}S for selective photocatalytic CO₂ reduction, *Chin. J. Catal.* 42 (2021) 131–140.

[40] W. Gao, S. Li, H. He, X. Li, Z. Cheng, Y. Yang, J. Wang, Q. Shen, X. Wang, Y. Xiong, Y. Zhou, Z. Zou, Vacancy-defect modulated pathway of photoreduction of CO₂ on single atomically thin AgInP₂S₆ sheets into olefiant gas, *Nat. Commun.* 12 (2021) 4747–4754.